machines

MDPI

Article

Structural Design and Random Vibration Analysis of a High-Stability Momentum Wheel

Yukuan Xie, Yuan Xue *, Hongxiang Wang and Yinjin Sun

School of Mechatronics Engineering, Harbin Institute of Technology, Harbin 150001, China
* Correspondence: xueyuan106@hit.edu.cn

Abstract: A novel expandable wheel body assembly is designed in this paper. The wheel body assembly utilizes the elastic deformation of the hub to clamp the bearing assembly. The gaps between them are effectively eliminated by this structure, improving the rotational precision and operational stability of the momentum wheel. A finite element model of the momentum wheel was established, and stress analysis was conducted using finite element analysis (FEA) software ANSYS 2025R1 to validate its mechanical integrity. The results demonstrate that the designed momentum wheel meets the required strength specifications. Additionally, the random vibration characteristics of the momentum wheel in a space environment were analyzed using ANSYS simulations, and a corresponding random vibration test was conducted. The good agreement between simulation and experimental results validates the reliability of the finite element model. The results indicate that this new type of momentum wheel can work reliably in aerospace conditions.

Keywords: wheel assembly; bearing assembly; momentum wheel; finite element analysis

check for updates

Academic Editor: Carmine Maria Pappalardo

Received: 24 March 2025
Revised: 9 May 2025
Accepted: 11 May 2025
Published: 13 May 2025

Citation: Xie, Y.; Xue, Y.; Wang, H.; Sun, Y. Structural Design and Random Vibration Analysis of a High-Stability Momentum Wheel. *Machines* **2025**, *13*, 406. https://doi.org/10.3390/machines13050406

Copyright: © 2025 by the authors. Licensee MDPI, Basel, Switzerland. This article is an open access article distributed under the terms and conditions of the Creative Commons Attribution (CC BY) license (https://creativecommons.org/licenses/by/4.0/).

1. Introduction

The momentum wheel (MW), also known as a biased flywheel, is a key actuator in spacecraft attitude control systems. It enables satellites to maintain or adjust their orientation by generating control torque through high-speed rotation [1–4]. However, during operation, MWs often experience high-frequency jitter caused by structural imbalance, leading to micro-vibrations. These micro-vibrations are a major source of disturbance in high-resolution satellites, significantly degrading the pointing accuracy and stability of the attitude control system and ultimately reducing imaging quality [5,6].

A momentum wheel primarily consists of a shell assembly, a wheel body assembly, a bearing assembly, a motor, and commutation circuitry [7,8]. Among these, the wheel body assembly and bearing assembly are the key components responsible for providing control torque. Most momentum wheels in current use feature an assembled wheel body structure, where the spokes, rim, and hub of the wheel body are joined through welding and screw connections. However, when operating in harsh space environments over extended periods, this structure suffers from insufficient connection stiffness and poor stability. Additionally, it fails to eliminate the contact gap between the hub and the bearing sleeve, leading to axial and radial vibrations during operation, which contribute to micro-vibrations in the momentum wheel [9].

To address these challenges, this paper proposes a novel integrated expandable wheel-body design for momentum wheels that eliminates welds and threaded joints to reduce assembly-induced deformation and enhance mechanical stiffness. The hub's controlled elastic deformation enables high-precision bearing clamping, removing fit

clearances and thus improving dynamic balance, vibration suppression, and resistance to mechanical shocks. The objectives of this work are to (1) develop a detailed structural design for the expandable wheel body, (2) evaluate its mechanical behavior through finite element simulations, and (3) validate its dynamic performance via random vibration tests at a rated speed of 5000 rpm under a 20–2000 Hz PSD profile to ensure an RMS acceleration below 70 g.

2. Wheel Assembly

There are two common structural types of wheel assemblies: assembled and integral. In an assembled wheel, the rim, spokes, and hub are made from different materials and assembled using welding, screws, or other connection methods. In contrast, an integral wheel is machined from a single piece of material, with the hub, spokes, and rim forming a unified structure. Compared to assembled wheels, integral wheels can effectively reduce deformation by eliminating the welding and threaded connections in traditional assembled momentum wheels; they also improve dynamic balance accuracy and are more suitable for the production of a single piece with enhanced resistance to impact and vibration.

This paper proposes an improved momentum wheel assembly with an expandable structure for high-precision bearing clamping. This design eliminates clearance between the hub and shaft sleeve, enhancing rotational accuracy while ensuring easy assembly, disassembly, and high reliability. The expandable wheel assembly is shown in Figure 1.

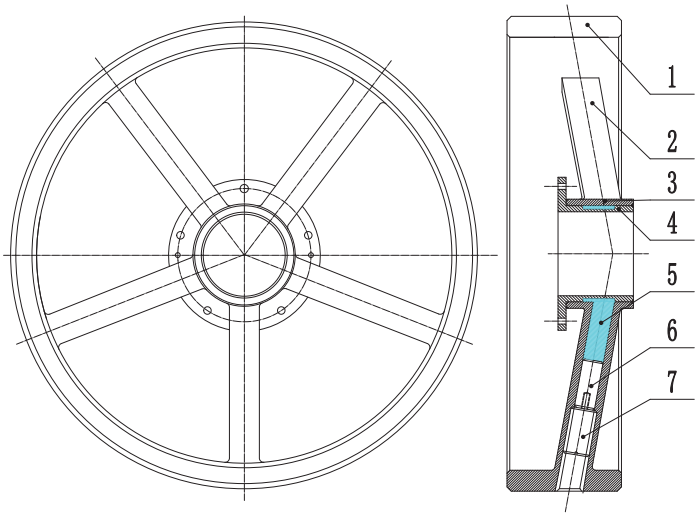


Figure 1. The structure of the expandable wheel assembly: 1. rim; 2. spokes; 3. outer ring of hub; 4. inner ring of hub; 5. elastomer; 6. push rods; 7. preload screws.

The expandable wheel assembly primarily consists of seven components: a rim, spokes, the outer ring of the hub, the inner ring of the hub, an elastomer, push rods, and preload screws. The rim, the spokes, and the outer ring of the hub, collectively referred to as the wheel body, are forged from 40CrNiMo quenched and tempered stainless steel blanks. After heat treatment, they are shaped through overall milling, during which the fan-shaped structure between the five spokes is removed. The hub's inner ring is designed with seven through holes, of which five are used to connect it to the bearing assembly and the other two are for positioning. The end faces of the hub inner ring and the wheel body are welded together to prevent the elastomer from leaking. The spoke-type wheel body has five spokes, each inclined at an angle of 9°. To facilitate processing, the cross-section of each spoke is designed with an outer square and an inner circular hollow structure. Each spoke is sequentially installed with an elastomer, push rod, and preload screw. When the set screw is tightened, it pushes the push rod to move radially within the spoke cavity, causing the elastomer to flow. The thin-walled

structure of the hub's inner ring deforms elastically under pressure, achieving high-precision clamping of the bearing assembly, as shown in Figure 2.

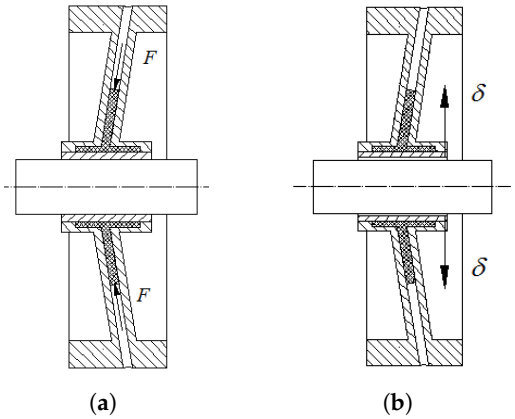


Figure 2. Expandable wheel assembly clamping schematic diagram. (**a**) Clamping the bearing assembly of the hub's inner ring. (**b**) Releasing the bearing assembly of the hub's inner ring.

3. Bearing Assembly

Momentum wheels mostly use high-precision angular contact ball bearings for support. The bearing assembly consists of two angular contact ball bearings installed back to back. It is essential for the bearing assembly to have good lubrication performance to reduce friction and wear, ensuring the long lifespan and high stability of the momentum wheel. The structure of the bearing assembly is shown in Figure 3.

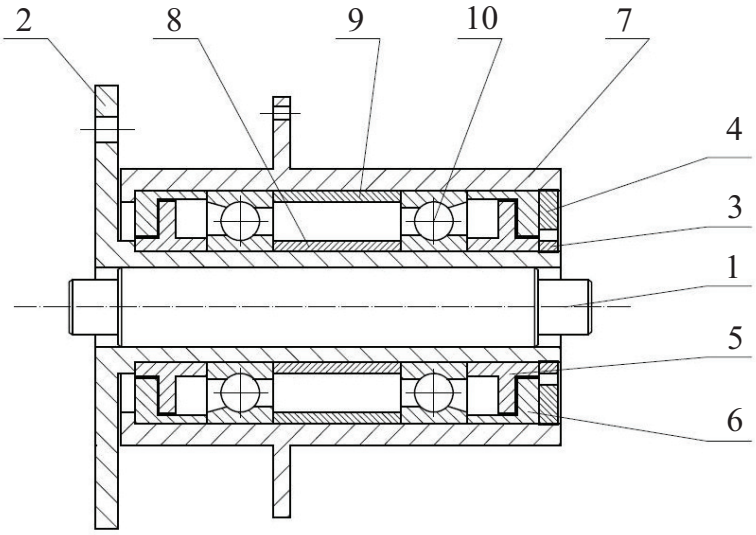


Figure 3. The structure of the bearing assembly: 1. spindle; 2. shaft sleeve; 3. inner retaining ring; 4. outer retaining ring; 5. inner locating sleeve; 6. outer locating sleeve; 7. bearing sleeve; 8. inner sleeve; 9. outer sleeve; 10. bearing.

4. Momentum Wheel

The motor and shell assembly are also essential components of the momentum wheel. Most existing momentum wheels utilize brushless DC motors, which feature a coreless stator design. These motors offer advantages such as long lifespan, high reliability, and low power consumption, fully meeting the technical requirements of satellite attitude control systems. The shell assembly is made of titanium alloy, which enhances the internal vacuum

level of the momentum wheel while also satisfying the weight reduction requirements of aerospace applications.

The expandable wheel body, bearing assembly, motor, and shell are assembled to form the expandable momentum wheel designed in this study; an overall model of its design is illustrated in Figure 4.

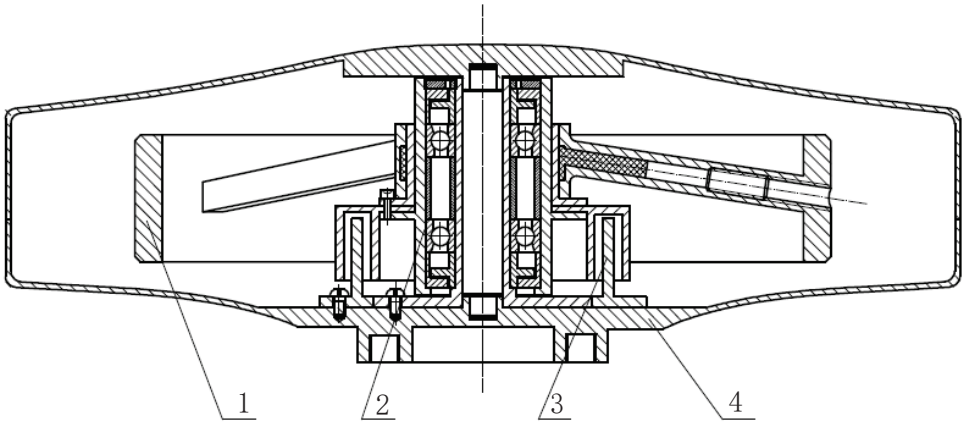


Figure 4. Overall model of the momentum wheel: 1. wheel body assembly; 2. bearing assembly; 3. motor; 4. shell assembly.

Figure 4 shows the main components of the expandable momentum wheel, including the expandable wheel body, bearing assembly, motor, and shell. During installation, the bearing assembly and motor rotor are first mounted onto the lower shell. The wheel body assembly is then installed onto the bearing sleeve, with the wheel hub secured using five screws. Subsequently, the radial positions of the five screws in the spokes are adjusted, applying pressure to the elastic bodies within the spokes. This pressure induces a slight elastic deformation in the inner hub ring, achieving high-precision clamping of the bearing assembly.

Additionally, the momentum wheel features an integral wheel body structure, which significantly enhances the strength of the wheel body and improves its resistance to impact and vibration in the complex dynamic environment of space. This design extends the operational lifespan of the momentum wheel and improves its overall performance in satellite attitude control applications. A physical diagram of the momentum wheel used in the subsequent tests is shown in Figure 5.



Figure 5. Physical diagram of the momentum wheel, not including the shell.

5. Finite Element Analysis

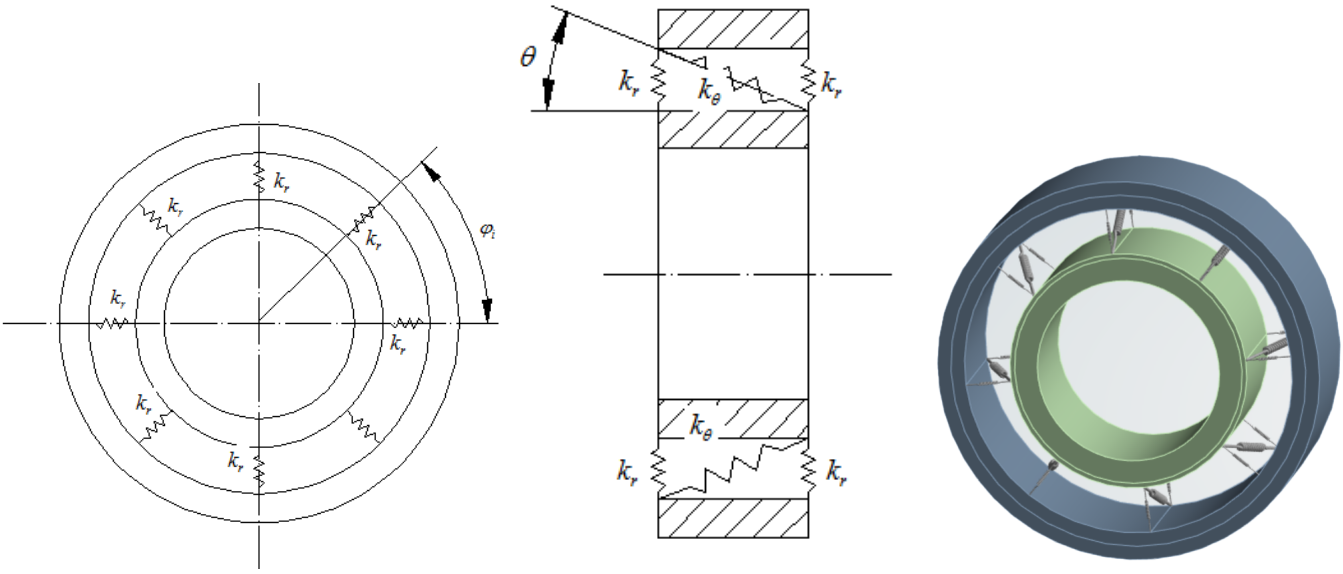
During spacecraft launch, the momentum wheel undergoes sustained acceleration, leading to mechanical stress and dynamic loads. To ensure its structural integrity and reliable operation, a strength analysis is necessary to assess potential deformations, material fatigue, and stress concentrations.

5.1. Simplification of the Finite Element Model of Angular Contact Ball Bearings

For support, the wheel body assembly uses a set of back-to-back angular contact ball bearings (B7004), which need to be simplified. The dimensional parameters of the angular contact bearings are provided in Table 1, with radial stiffness $K_r = 1.05 \times 10^8$ N/m and axial stiffness $K_a = 1.27 \times 10^7$ N/m [10]. In ANSYS, two radial and one inclined spring-damping unit (COMBIN14) are used to replace each bearing ball, with a total of eight sets. The tilt angle θ represents the bearing contact angle. The inner and outer rings of the bearing are retained. The simplified bearing model is shown in Figure 6.

Table 1. Dimensional parameters of angular contact ball bearings (B7004).

Outer Diameter (mm)	Inner Diameter (mm)	Radial Distance (mm)	Width (mm)	Ball Diameter (mm)	Number of Balls	Contact Angle (°)
20	42	31	12	6	11	15



(**a**) (**b**) (**c**)

Figure 6. The simplified bearing model. (**a**) 2D axial view; (**b**) 2D radial view; (**c**) 3D structure view.

The following section calculates the stiffness of the radial and inclined COMBIN14 spring-damping units based on the radial and axial stiffness of the bearing. According to the stiffness equivalence principle and the bearing simplification schematic, we have

$$\begin{cases} \sum_{i=1}^{8} \cos\varphi_i (2k_r + k_\theta \sin\theta) = K_r \\ \sum_{i=1}^{8} k_\theta \cos\theta = K_a \end{cases} \tag{1}$$

Solving these equations yields $k_r = 6.35 \times 10^6$ N/m, $k_\theta = 4.23 \times 10^6$ N/m.

5.2. Finite Element Model of the Momentum Wheel

In this study, ANSYS is used to conduct the mechanical analysis of the momentum wheel in an environment of constant acceleration. The momentum wheel consists of the wheel body assembly, bearing assembly, motor, and shell assembly. If a finite element model were established based on the actual structure of the momentum wheel, computational efficiency would be significantly reduced. In practice, small features such as screw holes, chamfers, and fillets have minimal impact on the overall FEA results of the momentum wheel. Therefore, details on the wheel body, bearing assembly, motor, and shell have been simplified. SOLID186 is a higher-order solid element suitable for meshing curved surfaces, making it the chosen element type for this study. The momentum wheel is meshed using tetrahedral elements. The material properties of each component of the momentum wheel are listed in Table 2. The finite element model of the expandable momentum wheel, comprising 264,328 nodes and 144,371 elements, is depicted in Figure 7.

Table 2. Material properties of each part of the momentum wheel.

Name	Material	Density (kg/m^3)	Elastic Modulus (MPa)	Poisson's Ratio	Yield Strength (MPa)
Wheel Body	40CrNiMo [11]	7.8×10^3	2.09×10^5	0.27	835
Shell	Titanium Alloy	4.45×10^3	1.14×10^5	0.34	668
Spindle	40Cr [12]	7.8×10^3	2.06×10^5	0.29	785
Bearing	9Cr18Mo [13]	7.7×10^3	2.22×10^5	0.3	696
Other Parts	Steel	7.8×10^3	2.10×10^5	0.3	$\geq$600

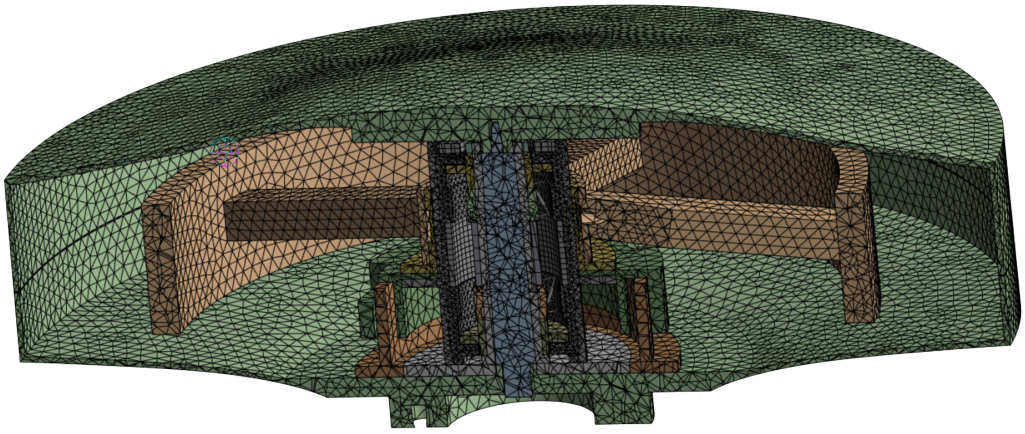


Figure 7. FEM model of the momentum wheel.

5.3. Structural Strength Analysis

To verify the structural strength of the momentum wheel under high-speed rotation, an FEA was conducted by applying a rotational speed of 10,000 rpm, which is twice the rated speed of 5000 rpm, in order to account for potential overload conditions. In addition, inertial acceleration loads equivalent to 10G were applied to the momentum wheel separately in the x, y, and z directions to simulate extreme conditions encountered during the launch phase of the spacecraft.

To reflect the actual installation constraints, a fixed boundary condition was applied to the bottom surface of the momentum wheel. The static structural system was used for the analysis. The simulation results for the von-Mises stress distribution under a rotational speed of 10,000 rpm are shown in Figure 8. The maximum von-Mises stress, 378.72 MPa, occurs at the junction between the spokes and the hub of the wheel body. The yield strength of the wheel body material is 835 MPa. Clearly, the maximum stress is well below the

yield limit, indicating that the structure meets the strength requirements. The momentum wheel can operate safely without fracture or failure both at the rated speed and under overspeed conditions.

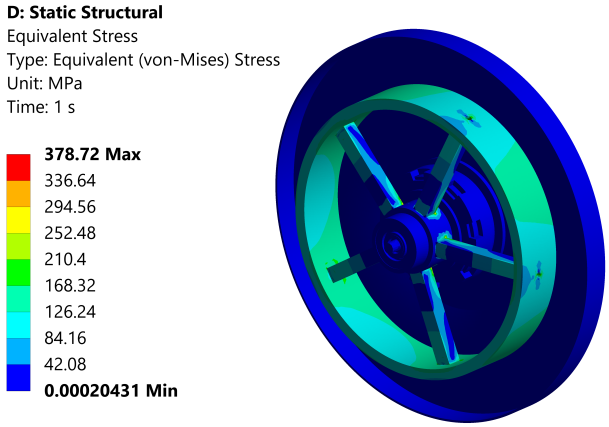
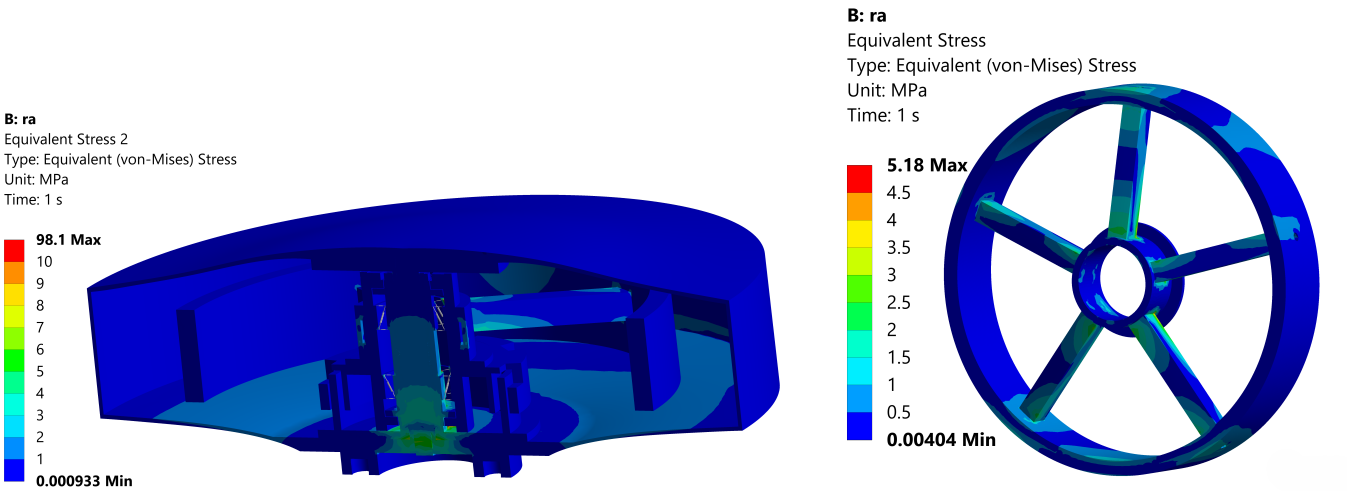


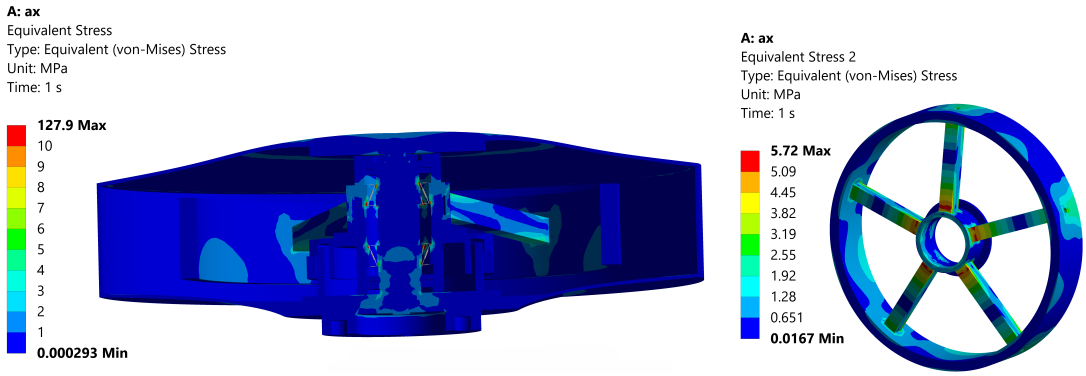
Figure 8. The von-Mises stress distribution of the momentum wheel body assembly at a rotational speed of 10,000 rpm.

The simulation results for the von-Mises stress distribution at a radial acceleration of 10G are shown in Figure 9. As shown in Figure 9a, the maximum overall stress of 98.1 MPa occurs at the connection between the inner and outer races of the bearing and the COMBIN14 units, where the COMBIN14 elements are employed to replace the physical characteristics of the bearing. As shown in Figure 9b, the maximum stress of 5.18 MPa in the wheel body assembly occurs at the connection between the spokes and the rim. The simulation results for the von-Mises stress distribution at a radial acceleration of 10G are shown in Figure 10. As shown in Figure 10a, the maximum overall stress of 127.9 MPa occurs at the connection between the inner and outer races of the bearing and the COMBIN14 units. As shown in Figure 10b, the maximum stress of 5.72 MPa in the wheel body assembly occurs at the connection between the spokes and the outer hub ring. Thus, the momentum wheel can operate safely and reliably in a constant-acceleration environment.



(**a**) (**b**)

Figure 9. The von-Mises stress distribution under a 10G radial load. (**a**) Overall sectional view; (**b**) Wheel body assembly view.



(**a**) (**b**)

Figure 10. The von-Mises stress distribution under a 10G axial load. (**a**) Overall sectional view; (**b**) Wheel body assembly view.

Additionally, a sensitivity analysis was conducted by varying the mesh density from coarse to fine. It was observed that the stress at the COMBIN14 elements increased with mesh refinement, primarily due to the enhanced resolution of local stress concentrations. Nevertheless, the average stress in the critical regions remained stable at ±3%, demonstrating that the simulation results are convergent and the finite element calculations are reliable.

5.4. Modal Analysis

To further conduct dynamic response analysis, a constrained modal analysis was performed on the momentum wheel with the bottom surface fixed, simulating the actual installation condition. The first six natural frequencies are 0 Hz, 155.31 Hz, 155.32 Hz, 314.08 Hz, 314.19 Hz, and 413.26 Hz. The first natural frequency of the momentum wheel is 0 Hz, indicating the existence of a rotational degree of freedom due to the simplified modeling of angular contact bearings. The first nonzero natural frequency is 155.31 Hz, which meets the requirement of being higher than the rated rotational speed (83 Hz, 5000 rpm). It is also observed that the second and third natural frequencies are identical, as are the fourth and fifth natural frequencies, primarily due to the symmetric structure of the momentum wheel. The corresponding mode shapes are shown in Figure 11.

The first mode shape corresponds to the rotation of the wheel assembly around the main axis; the second and third mode shapes correspond to the swinging of the wheel assembly in the xz and yz planes, respectively; the fourth and fifth mode shapes correspond to the swinging of the shell in the xz and yz planes; and the sixth mode shape corresponds to the rigid axial translation of the wheel assembly.

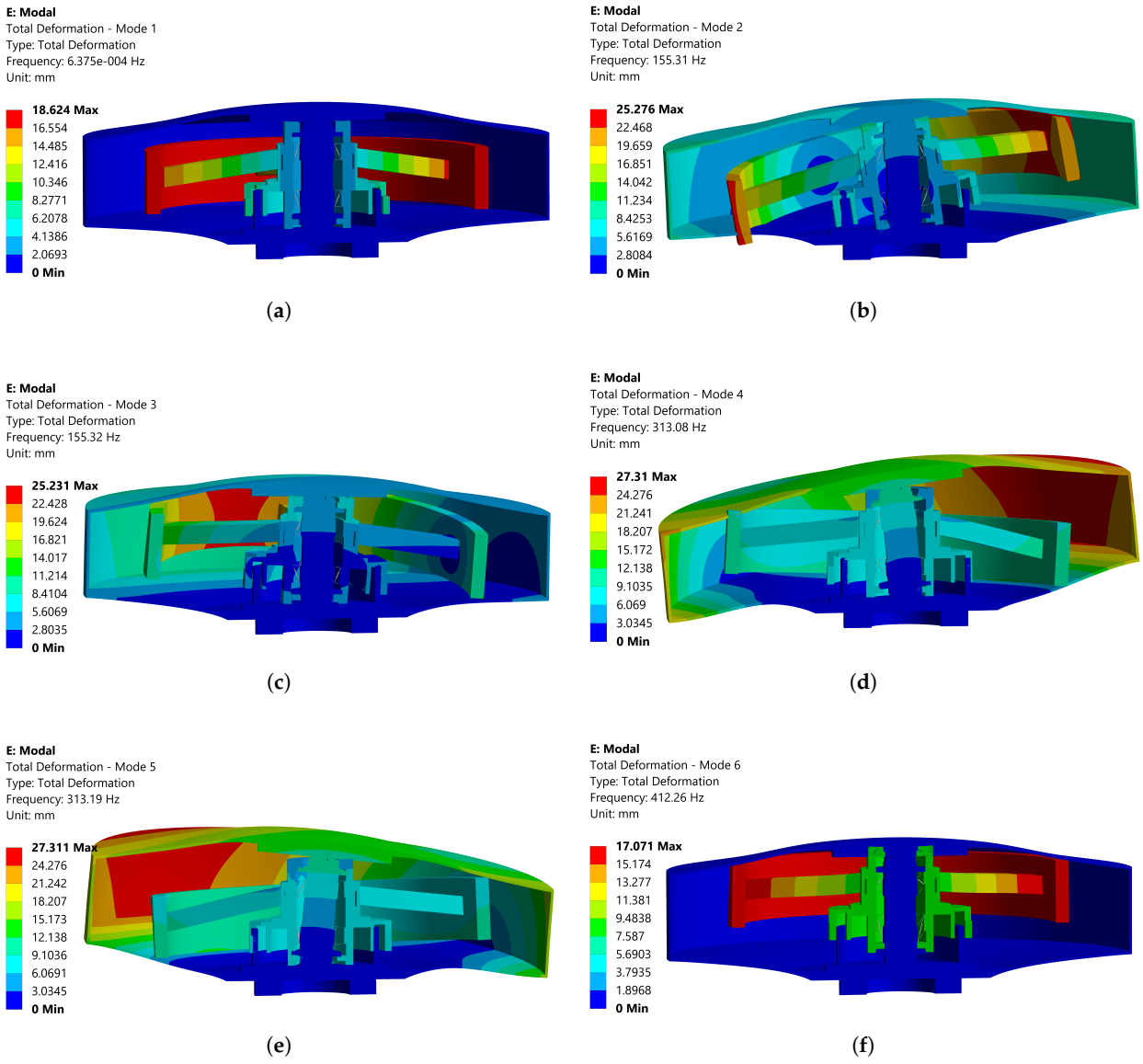


Figure 11. Mode shapes of the first six orders: (**a**) 0 Hz; (**b**) 155.31 Hz; (**c**) 155.32 Hz; (**d**) 314.08 Hz; (**e**) 314.19 Hz; (**f**) 413.26 Hz.

6. Random Vibration Response Analysis

Random vibration is a type of dynamic environment vibration, primarily originating from launch exhaust noise and aerodynamic noise during flight, with a frequency range of approximately 20–2000 Hz [14,15]. This vibration environment can dynamically propagate to the structural or instrumental levels of spacecraft, including system-level, subsystem-level, or component-level structures. It may cause structural damage, leading to performance degradation or even failure of instruments and equipment, posing significant threats to the safe operation of spacecraft [16].

Therefore, this section conducts a random vibration test on the momentum wheel to verify its reliability in an environment with random vibration.

6.1. Analysis of Frequency Characteristics of Random Vibration

Let $f(t)$ be the random vibration excitation applied to the system in the time domain. According to Parseval's theorem, it can be transformed into the frequency domain as follows:

$$\int_{-\infty}^{+\infty} |f(t)|^2 dt = \frac{1}{2\pi} \int_{-\infty}^{+\infty} |F(\omega)|^2 d\omega \tag{2}$$

where $F(\omega)$ is the random vibration excitation in the frequency domain.

By applying the Fourier transform to the autocorrelation function $R_x(\tau)$, we obtain

$$S_x(\omega) = \int_{-\infty}^{+\infty} R_x(\tau) e^{-i\omega\tau} d\tau \tag{3}$$

where $S_x(\omega)$ is the power spectral density (PSD) function of the random vibration.

The inverse transform of this equation is

$$R_x(\tau) = \frac{1}{2\pi} \int_{-\infty}^{+\infty} S_x(\omega) e^{i\omega\tau} d\omega \tag{4}$$

Equations (3) and (4) form a Fourier transform pair, which is known as the Wiener–Khinchin theorem.

For Equation (4), if we set $\tau = 0$, then

$$R_x(0) = \frac{1}{2\pi} \int_{-\infty}^{+\infty} S_x(\omega) d\omega \tag{5}$$

It is known that the autocorrelation function satisfies

$$R_x(0) = \psi_x^2 \tag{6}$$

where ψ_x^2 is the mean square value of the random vibration, which represents the total energy of the random vibration.

From Equations (5) and (6), we obtain

$$\psi_x^2 = R_x(0) = \frac{1}{2\pi} \int_{-\infty}^{+\infty} S_x(\omega) d\omega \tag{7}$$

From the above equations, the PSD function $S_x(\omega)$ represents the distribution of the mean square value of the random vibration in the frequency domain. In other words, the PSD function $S_x(\omega)$ indicates the energy distribution across frequencies [17].

6.2. Statistical Characteristics of Random Vibration Response

The response of a linear system under any excitation can be obtained using the convolution integral:

$$x(t) = \int_0^t F(\tau) h(t-\tau) d\tau \tag{8}$$

Extending the integration limits of Equation (8) to $-\infty$ and $+\infty$ does not affect the result, yielding

$$x(t) = \int_{-\infty}^{+\infty} F(\tau) h(t-\tau) d\tau \tag{9}$$

Let $F(t)$ be the random vibration excitation applied to the system, and let $x(t)$ be its response.

The autocorrelation function of the random vibration response is given by

$$R_x(\tau) = E[x(t)x(t+\tau)] \tag{10}$$

After calculation, the PSD of the random vibration response is

$$S_x(\omega) = |H(\omega)|^2 S_F(\omega) \tag{11}$$

where $S_F(\omega)$ is the PSD of the random vibration excitation, while $H(\omega)$ is the system's frequency response function.

The mean square value of the response is

$$\psi_x^2 = R_x(0) = \int_{-\infty}^{+\infty} S_x(\omega) d\omega = \int_{-\infty}^{+\infty} S_F(\omega) |H(\omega)|^2 d\omega \tag{12}$$

From Equation (12), it is evident that, given the PSD of the random vibration excitation and the system's frequency response function, the random vibration response of the system can be determined.

When the system is subjected to multiple independent and uncorrelated random vibration excitations, the total response PSD $S(\omega)$ is the sum of the power spectral densities of all the excitation responses:

$$S(\omega) = \sum |H_i(\omega)|^2 S_{F_i}(\omega) \tag{13}$$

Equation (13) indicates that the system's random vibration response depends not only on external excitations but also on the system's inherent characteristics. In random vibration response analysis, studying the relationship between applied random vibration excitation and the system's response can reveal structural characteristics and assess the reliability of the structure [18].

6.3. Random Vibration Experiment

To verify the reliability of the expandable momentum wheel and assess its ability to withstand environments of vibration, a random vibration test was conducted using specialized equipment to simulate the vibration environment of space. Prior to the experiment, a dynamic balancing test was performed on the momentum wheel, achieving a static imbalance of 122 mg·cm and a dynamic imbalance of 693 mg·cm². The wheel was then sealed and subjected to a vacuum treatment.

The momentum wheel was mounted onto the vibration table using bolts. The acceleration was measured at two points: measurement point A1 was placed at the crown top of the shell, and measurement point A2 was located on the welded band of the shell side. Additionally, a control point was placed on the base of the momentum wheel to provide feedback on the vibration conditions applied by the vibration table. A schematic diagram is shown in Figure 12. According to the design requirements, the acceleration PSD curves for random vibration in the x, y, and z directions are depicted in Figure 13, with a sweep duration of 1 min.

The control spectral curves for the random vibration test are shown in Figure 14, where the AlarmHigh curve represents the upper tolerance band, the AlarmLow curve represents the lower tolerance band, and the Control curve is the actual control spectral curve. The region between the AlarmLow and AlarmHigh curves defines the allowable error range. Since the acceleration PSD curves for the x and y directions at the control point are identical, the y-direction control spectral curve is omitted. As observed in Figure 14, the control spectral curves for the x and z directions fall within the tolerance band, indicating that the applied test conditions are within the allowable error range.

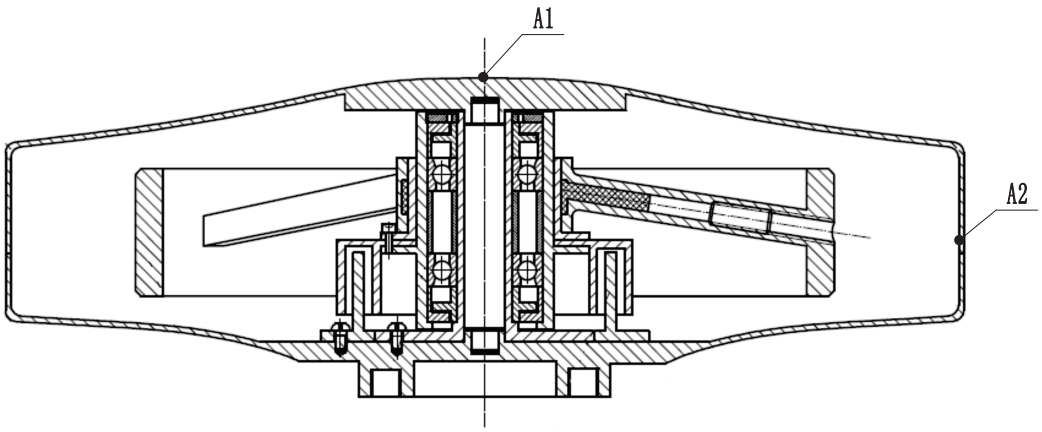


Figure 12. Measurement points.

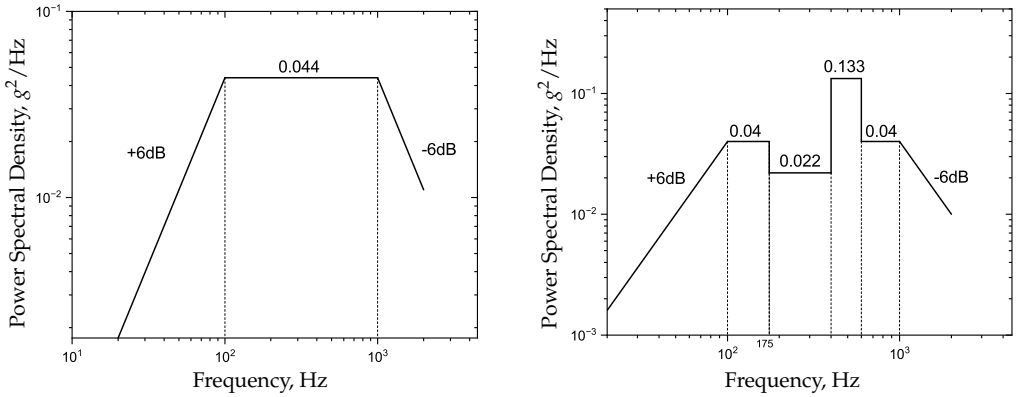


Figure 13. PSD of random vibration in different directions: (**a**) x/y directions; (**b**) z direction.

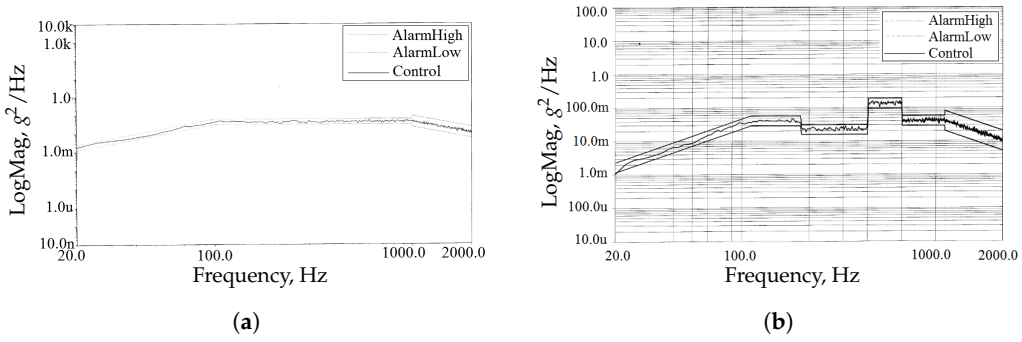


Figure 14. Control spectrum: (**a**) x direction; (**b**) z direction.

The raw response spectral data at measurement points A1 and A2 in the x, y, and z directions are shown in Figures A1, A2, and A3, respectively. For comparative reference, these data are re-plotted in Figures 15 and 16, where each curve labeled with -Test represents the result of random vibration testing.

The maximum and total root mean square (RMS) acceleration responses at each measurement point were statistically evaluated using the raw acceleration data, as summarized in Table 3.

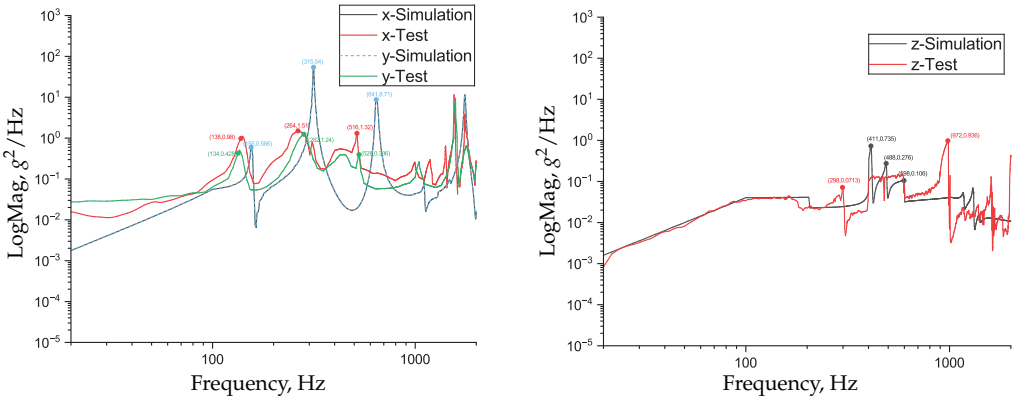


Figure 15. Measurement point A1—response spectrum of random vibration test and FEA simulation: (**a**) x/y directions (the x- and y-Simulation results are overlapping); (**b**) z direction.

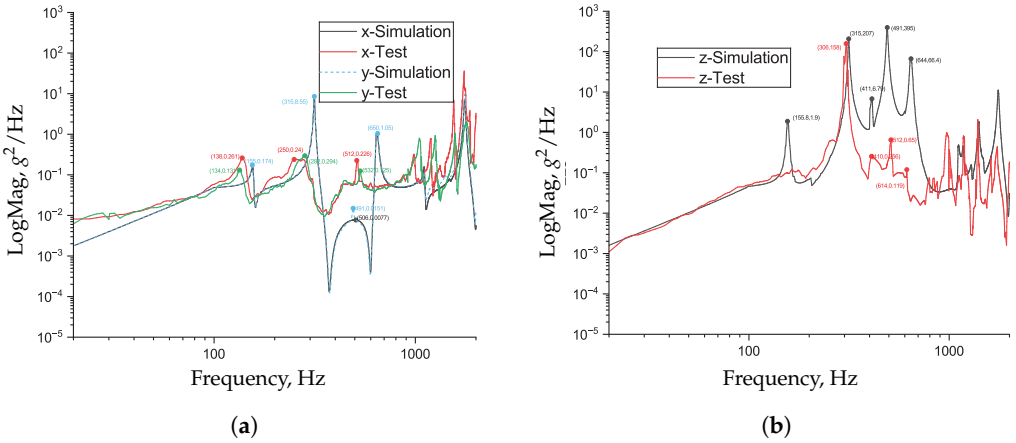


Figure 16. Measurement point A2—response spectrum of random vibration test and FEA simulation; (**a**) x/y directions (the x- and y-Simulation results are overlapping); (**b**) z direction.

Table 3. Acceleration response statistics.

Excitation Direction	Measurement Point	Maximum Response Acceleration		Total RMS Response (g)
		Peak Value (g^2/Hz)	Frequency (Hz)	
x	A1 (Crown Top)	29.10	1541	34.50
	A2 (Weld Band)	22.33	1734	41.53
y	A1 (Crown Top)	8.841	1543	24.20
	A2 (Weld Band)	2.169	1740	22.40
z	A1 (Crown Top)	0.936	972	10.39
	A2 (Weld Band)	220.5	305	39.80

From Table 3, it can be seen that under x-direction excitation, the maximum response accelerations at measurement points A1 and A2 are significantly greater than those under y- and z-direction excitation. However, under z-direction excitation at 305 Hz, the response acceleration at measurement point A2 reaches 220 g^2/Hz. Furthermore, the total RMS response under x-direction excitation is also considerably higher than in the other two directions, with the highest total RMS response of approximately 41.53 g occurring at A2. According to the space dynamic environment specifications provided by the project, the RMS acceleration response required for the reliable operation of the momentum wheel is

70 g. The analysis results demonstrate that the momentum wheel satisfies this requirement, indicating that it meets the random vibration response criteria for space applications.

Following the vibration test, the expandable momentum wheel was disassembled for inspection. No fractures, permanent deformations, or other forms of damage were observed in critical components—including the wheel body, main shaft, bearings, and bushings—further confirming that the expandable momentum wheel meets both the strength and reliability requirements.

6.4. Random Vibration Simulation

To validate the accuracy and dynamic fidelity of the finite element model, a random vibration FEA was performed based on the preceding modal analysis (Section 5.4) and the specified PSD inputs (Figure 13), which were applied to the fixed support located at the bottom surface of the momentum wheel. The results are also plotted in Figures 15 and 16, where each curve labeled with -Simulation represents the numerical response predicted by the FEA.

The simulation results exhibit a similar overall trend to the experimental data. While noticeable differences can be observed in the amplitude of the peak responses, the corresponding peak frequencies remain closely aligned between the test and the simulation. Particular attention is given to the first nine modes under 700 Hz; their peak frequencies and mode shapes are summarized in Table 4.

Table 4. Comparison of modal frequencies with peak frequencies from random vibration testing and simulation response spectrum. '–' indicates the absence of a peak for this mode in the specified direction. (Unit: Hz).

Mode No.	Modal Analysis	Mode Shape	A1: x/y Directions		A1: z Direction		A2: x/y Directions		A2: z Direction	
			Sim.	Test	Sim.	Test	Sim.	Test	Sim.	Test
1	0	Rotation of wheel assembly	–	–	–	–	–	–	–	–
2/3	155.8	Swing of wheel assembly in xz and yz planes	154	134/138	–	–	155	134/138	155	–
4/5	314.4	Swing of housing in xz and yz planes	315	264/282	–	298.2	315	250/282	315	306
6	413.1	Translation of wheel in z direction	–	–	411	–	–	–	411	410
7	490.1	Translation of housing in z direction	–	–	488	–	491/506	–	491	512
8/9	639.4	Swing of housing/wheel assembly in z direction	641	516/528	–	–	650	512/532	644	614

As shown in Figures 15 and 16 and Table 4, the resonant frequencies obtained from the test are generally lower than those predicted by the simulation. This may be partially attributed to the absence of damping modeling in the finite element analysis (FEA), although damping primarily affects response amplitudes rather than frequency positions. The higher peak amplitudes in the simulation are also consistent with the lack of damping.

In the x and y directions, the test frequencies are, on average, 16 ± 5% lower than the simulated natural frequencies, indicating reasonably good correlation. Furthermore, the z-direction response at measurement point A2 shows that the simulated and measured frequencies are closely matched, which suggests that the axial damping is relatively small. This observation is consistent with the physical characteristics of the system: the momentum wheel mainly rotates about its axis, resulting in significant radial loads due to centrifugal forces and bearing friction. These loads lead to higher radial damping. In contrast, the axial direction typically allows a small amount of clearance in the bearing design, resulting in lower contact pressure and lesser damping, as the axial load is mainly supported by the thrust-bearing components.

Nevertheless, at certain locations, discrepancies between the simulation and experimental peak frequencies are observed. These are likely caused by simplifications in the geometric model—such as the omission of motors or other components—and the idealized modeling of joint stiffness or preload. In practice, effects such as local looseness, contact nonlinearity, or coupling with unmodeled components can lead to additional localized vibration modes not captured in the simulation.

Overall, the frequency positions and distribution trends observed in the random vibration test are largely consistent with the simulation results, validating the rationality of the model's stiffness and mass distribution. Although some discrepancies in amplitude response remain, they are most likely due to uncertainties in damping parameters and simplifications of local structural details.

7. Conclusions

A novel expandable momentum wheel was independently designed, utilizing the elastic deformation of the hub to achieve high-precision clamping of the bearing sleeve. This design effectively reduces the vibratory force generated during rotation, thereby enhancing the stability of the momentum wheel in the dynamic environment of space while improving its impact resistance and overall reliability. Based on the stiffness equivalence principle, a finite element model of the momentum wheel was established by simplifying the finite element model of the angular contact ball bearing, and its static mechanical response at an overloaded rotational speed of 10,000 rpm under a constant acceleration of 10G was analyzed. The results indicate that the designed momentum wheel satisfies the strength requirements of the launch process, with a maximum von-Mises stress of 378.5MPa. Furthermore, a random vibration finite element analysis was conducted by applying a reasonable acceleration power spectral density to simulate the random vibration environment of space. A random vibration test was first conducted, and the acceleration response spectra at two measurement points were obtained. Finite element analysis (FEA) was subsequently performed for comparison. The results showed a consistent trend between the test and FEA in the low-frequency range, with the peak frequencies in the x and y directions differing by 16% ± 5% between the experimental and simulated results, thereby validating the effectiveness of the FEA model. Furthermore, the analysis confirmed that the designed momentum wheel meets the strength requirements to withstand the random vibration conditions found on spacecraft.

Author Contributions: Methodology, Y.X. (Yukuan Xie) and Y.X. (Yuan Xue); Validation, H.W. and Y.S. All authors have read and agreed to the published version of the manuscript.

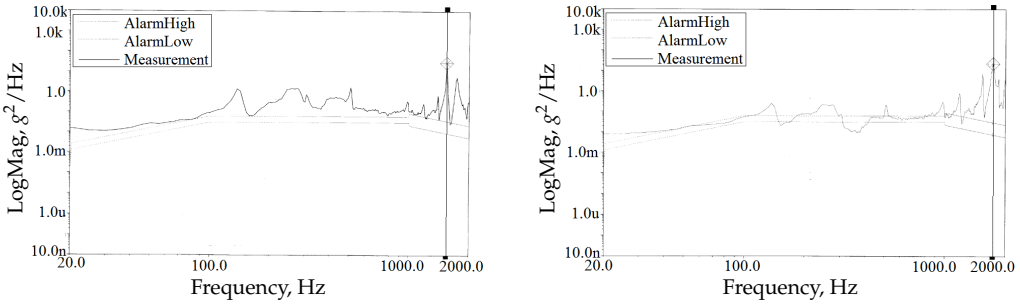
Funding: This research received no external funding

Data Availability Statement: Data are contained within the article.

Conflicts of Interest: The authors declare no conflicts of interest.

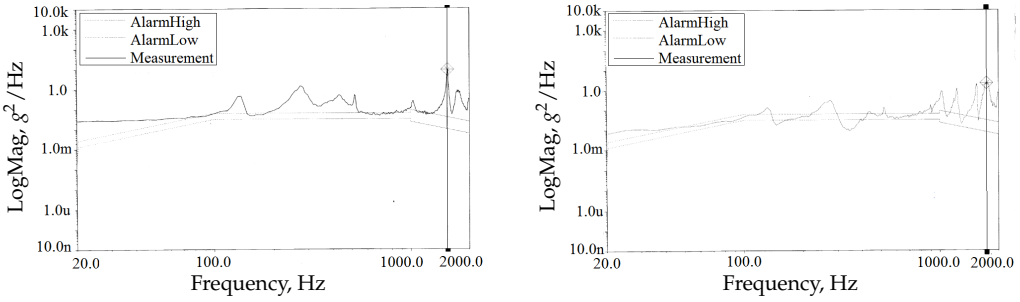
Appendix A

The raw data from the random vibration test are shown in Figures A1, A2, and A3, respectively.



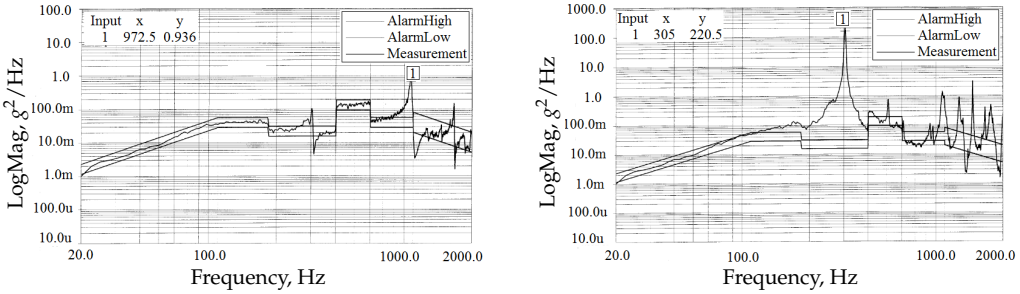
(**a**) (**b**)

Figure A1. Raw data of x response spectrum. (**a**) Measurement point A1. (**b**) Measurement point A2.



(**a**) (**b**)

Figure A2. Raw data of y response spectrum. (**a**) Measurement point A1. (**b**) Measurement point A2.



(**a**) (**b**)

Figure A3. Raw data of z response spectrum. (**a**) Measurement point A1. (**b**) Measurement point A2.

References

1. Huang, H.Z.; Yu, K.; Huang, T.; Li, H.; Qian, H.M. Reliability estimation for momentum wheel bearings considering frictional heat. *Eksploat. Niezawodn.-Maint. Reliab.* **2020**, *22*, 6–14. [CrossRef]
2. Kasiri, A.; Fani Saberi, F. Optimal Configuration of Four Reaction Wheels in Momentum Management Performance and Reliability Point of View. *Iran. J. Sci. Technol.-Trans. Mech. Eng.* **2023**, *47*, 2021–2043. [CrossRef]
3. Grotte, M.E.; Gravdahl, J.T.; Johansen, T.A. A Constrained Control Allocation and Tuning Scheme for Hybrid Actuators in Spacecraft Attitude Control. *IFAC Pap.* **2023**, *56*, 11273–11280. [CrossRef]
4. Li, Y.F.; Huang, M.; Bai, S.; Chen, Y.; Huang, H.Z. Reliability Modeling and Analysis of Multi-Degradation of Momentum Wheel Based on Copula Function. *Appl. Sci.* **2021**, *11*, 11563. [CrossRef]
5. Wang, D.; Li, L.; Tan, L.; Kong, L.; Yang, H. Flywheel micro-vibration characters of a high resolution optical satellite. *J. Vibroengineering* **2017**, *19*, 3981–3993. [CrossRef]
6. Wang, Y.B.; Qian, Y.J.; Wang, Y.W.; Yang, X.D.; Xu, L. Flutter analysis of a rigid-flexible coupled composite space structure with momentum wheels under thermal load. *Aerosp. Sci. Technol.* **2024**, *148*, 109114. [CrossRef]
7. Luhang, L.; Qiang, Z.; Hong, W.; Gang, L.; Hao, W.; Zhipeng, W.; Baozhu, G.; Jiyang, Z. Fault diagnosis for momentum wheel bearing based on spectral kurtosis entropy and hierarchical extreme learning machine. *Chin. Space Sci. Technol.* **2021**, *41*, 97–104. [CrossRef]

8. Xiao, H.; Liu, Z.; Zhang, R.; Kelham, A.; Xu, X.; Wang, X. Study of a novel rotational speed amplified dual turbine wheel wave energy converter. *Appl. Energy* **2021**, *301*, 117423. [CrossRef]
9. Wan, Q.; Liu, G.; Shi, H.; Zhang, X.; Ning, X. Analysis of dynamic characteristics for momentum wheel assembly with joint clearance. *Adv. Mech. Eng.* **2018**, *10*, 168781401881891. [CrossRef]
10. Liu, J.; Tang, C.; Wu, H.; Xu, Z.; Wang, L. An Analytical Calculation Method of the Load Distribution and Stiffness of an Angular Contact Ball Bearing. *Mech. Mach. Theory* **2019**, *142*, 103597. [CrossRef]
11. Karimbaev, R.; Pyun, Y.-S.; Maleki, E.; Unal, O.; Amanov, A. An Improvement in Fatigue Behavior of AISI 4340 Steel by Shot Peening and Ultrasonic Nanocrystal Surface Modification. *Mater. Sci. Eng. A* **2020**, *791*, 139752. [CrossRef]
12. *GB/T 3077-2015*; Alloy Structural Steels. China Standards Press: Beijing, China, 2015. Available online: http://www.sac.gov.cn (accessed on 24 March 2025).
13. Zheng, C.; Fu, B.; Tang, Y.; Kong, L.; Wang, Y.; Li, N. Microstructure and Mechanical Properties of 9Cr18Mo Martensitic Stainless Steel Fabricated by Strengthening-Toughening Treatment. *Mater. Sci. Eng. A* **2023**, *869*, 144783. [CrossRef]
14. Calvi, A. Reduction of Overtesting during Base-Drive Random Vibration Tests for the Euclid Spacecraft Hardware. In Proceedings of the European Conference on Spacecraft Structures, Materials and Environmental Testing, Braunschweig, Germany, 1–4 April 2014; pp. 167–180. [CrossRef]
15. Wu, Q.; Li, D. Analysis on pseudo excitation of random vibration for structure of time flight counter. *Chin. J. Mech. Eng.* **2014**, *28*, 325–330. [CrossRef]
16. Pylypenko, V, O.; Khoroshylov, V, S.; Nikolayev, D.O. Development of vibration protection systems of spacecraft—state of the art and perspectives. *Space Sci. Technol.-Kosm. Nauka Tehnol.* **2023**, *29*, 3–19. [CrossRef]
17. Chen, J.; Kong, F.; Peng, Y. A stochastic harmonic function representation for non-stationary stochastic processes. *Mech. Syst. Signal Process.* **2017**, *96*, 31–44. [CrossRef]
18. Xiao, X.; He, Z.; Zhu, Q.; Ren, W. Analytical Study on Response Power Spectral Density of Structures Subjected to Nonstationary Excitation Considering Transient Responses. *J. Eng. Mech.* **2024**, *150*, 04023112.

Disclaimer/Publisher's Note: The statements, opinions and data contained in all publications are solely those of the individual author(s) and contributor(s) and not of MDPI and/or the editor(s). MDPI and/or the editor(s) disclaim responsibility for any injury to people or property resulting from any ideas, methods, instructions or products referred to in the content.